

Numerical Analysis of Fluid–solid Interactions in a 3D Piezoelectric Micropump Featuring a Passive Check Valve

Y. F. Zhang, B. Zhou, and Z. L. Deng[†]

School of Energy and Environment, Southeast University, Nanjing, Jiangsu, 210096, China

[†]Corresponding Author Email: zldeng@seu.edu.cn

ABSTRACT

Piezoelectric micropumps have attracted considerable research attention due to their low production cost, compact size, and controllable output performance. However, the fluid-structure interaction mechanisms in passive check valve-based piezoelectric micropumps remain insufficiently understood, leading to gaps in the current understanding of how their flow characteristics influence overall performance. This study addresses these gaps by establishing a flow model for a typical cantilever valve piezoelectric micropump, considering the effects of fluid-structure interaction. Numerical simulations were performed to investigate the flow field, pressure distribution within the pump chamber, and the dynamic behavior of the check valve during operation. The simulations revealed that the mechanical inertia of the valve causes its opening to lag behind the fluid pressure wave propagation, leading to a phase difference between the piezoelectric actuator and the valve. This delay results in transient backflow during the valve's state transition, which negatively impacts the micropump's overall performance by reducing efficiency. Furthermore, the influences of valve dimensions, pump chamber size, piezoelectric actuator size, as well as external driving voltage and frequency on the pump's operational characteristics were systematically analyzed and optimized. Following the optimization process, the micropump's output flow rate increased to 34.02 mL/min, representing a 54.54% improvement over its initial design, demonstrating the substantial performance gains achieved through structural refinement.

Article History

Received October 7, 2024
Revised February 11, 2025
Accepted February 27, 2025
Available online May 5, 2025

Keywords:

Piezoelectric micropump
Passive check valve
Fluid-structure interactions
Multiphysics
Optimization

1. INTRODUCTION

The advancement of MEMS technology has accelerated the rapid progression of associated microfluidic technology (Lu et al., 2020). Micropumps, often considered the heart of microfluidics (Senjanović et al., 2016), have attracted increased attention from researchers and technicians because of their extensive application prospects in fields such as microelectronic cooling, chemistry, biomedicine, and medicine (Kaçar et al., 2020; Liu et al., 2020; Bußmann et al., 2021). Among these, piezoelectric micropumps, which utilize piezoelectric materials as the driving element, represent one of the various types of microfluidic pumps. These micropumps are distinguished by their straightforward structure, high precision, swift response, and excellent integrability (Wang & Fu, 2018; Li et al., 2019; Mohith et al., 2019; Wang et al., 2019). These characteristics render them suitable for supporting production in small mobile devices, medical instruments, engineering vehicles, and

avionics systems. Their role is particularly critical in pharmaceutical systems, where precise and reliable fluid control is paramount (Cui et al., 2008; Bui et al., 2017; Sakuma et al., 2017; Yeming & junyao, 2019).

Piezoelectric micropumps can be classified by structural design into valved and valveless types based on the basis of the configuration, single-chamber and multichamber types on the basis of the chamber structure, and membrane-driven and stack-driven types on the basis of the piezoelectric transducer configuration. Owing to the complex structure and high cost of multichamber pumps, as well as major fluid pulsation issues during operation, most piezoelectric pumps continue to utilize a single-chamber structure (Liu et al., 2010; Dong et al., 2017). Membrane-driven micropumps offer advantages such as compact size, light weight, and ease of fabrication, making them particularly suitable in light of the trend toward miniaturization in micropump design (Cazorla et al., 2016; Bayazidi et al., 2023). While valveless piezoelectric pumps feature a simpler structure and longer lifespan than their valved counterparts do, the absence of

NOMENCLATURE			
E	electrostatic field	u	velocity
F	force	V	electric potential
I	identity tensor	$V_{in/out}$	cumulative inlet/outlet fluid intake
n	outward normal direction	X	x-direction position
p	pressure	ε	Lagrangian strain tensor
Q	volumetric flow rate	θ	phase
Re	Reynolds number	μ	dynamic viscosity
rm	ramp function	ρ	density
S	Piola-Kirchhoff stress	ρ_v	volume charge density
t	time		

valves to control fluid direction leads to severe liquid backflow and low volumetric efficiency, significantly limiting their output capability (Zhang & Eitel, 2013; Singh et al., 2015; Zhao et al., 2019; Asadi et al., 2020). Valved piezoelectric pumps, which incorporate one-way valves at both the inlet and outlet channels, achieve directional fluid flow through the sequential opening and closing of these valves. Depending on the method used to control the valves, valved micropumps can be categorized into active and passive types. Given the intricate nature and potential reliability concerns of the control system for micropumps using active valves (Lee et al., 2004), the membrane-driven passive valve single-chamber piezoelectric pump stands out as a superior choice for high-precision microfluidic transport applications, particularly in the context of ongoing research aimed at minimizing the structural scale and achieving high-precision output.

Passive valve piezoelectric pumps can be categorized by valve type into ball valves, cantilever valves, wheel valves, umbrella valves, and others. Carrozza et al. (1995) introduced a micropump design utilizing a ball valve fabricated through a single stereolithography process, this pump features a long lifespan and is easy to fabricate, but its flow output efficiency is relatively low. Zeng et al. (2016) proposed a micropump utilizing a rubber umbrella valve, achieving a maximum output of 318 mL/min at a driving frequency of 80 Hz. However, with increasing frequency, the effects subsequent to the activation of the umbrella valve become increasingly significant. Dong et al. (2017) and Yang et al. (2006) proposed cantilever-valve-based piezoelectric pumps, which achieved maximum outputs of 2184.7 mL/min and 85.3 mL/min, respectively. Dong J. S. et al. optimized the valve flap thickness, determining the optimal thickness to be 0.188 mm, whereas Yang X. et al. designed a micropump with a power consumption of only 3.18 mW. However, cantilever valves are prone to fatigue, with phase lag occurring at high frequencies.

In addition to experimental research, numerical simulations offer valuable insights into the operational mechanisms of piezoelectric micropumps. Wang et al. (2006) employed finite element analysis to simulate and optimize the pump chamber diameter and piezoelectric transducer size, providing guidance for micropump design. However, many other geometric structure parameters of the micropump have not been addressed. Sayar and Farouk (2012) developed a multiphysical field coupling analysis model for numerically predicting the

performance of valveless piezoelectric micropumps, facilitating the optimization of MEMS-based micropump designs. Dau and Dinh (2015) performed a numerical study on PZT-driven valveless microblowers, creating a lumped model to investigate blower geometry and PZT diaphragm material. Gidde et al. (2020) identified the optimal structural parameters for the optimized design of valveless micropumps, achieving a peak back pressure of 200 Pa. Moreover, several other numerical simulations have been documented in the literature (Johari & Majlis, 2008; Kang & Auner, 2011; Kaviani et al., 2014).

A review of the literature reveals that despite numerous advancements in the numerical analysis of valveless piezoelectric pumps, few studies have focused on the numerical simulation of piezoelectric micropumps incorporating passive check valves. This scarcity is largely attributed to the inherent complexity of multiphysical coupling. This paper employs a bidirectional fluid–structure interaction (the interaction between the fluid dynamics (the flow of the fluid within the pump) and the solid mechanics (deformation and movement of the valve) within the system) numerical simulation method to thoroughly analyze the interplay between the micropump and the fluid. It optimizes the design of a cantilever-valve-based piezoelectric micropump, providing an optimal set of design parameters and examining its output flow and backpressure characteristics. The research outcomes presented herein provide valuable reference points for the design and practical application of cantilever-valve-based piezoelectric micropumps.

2. NUMERICAL MODEL

2.1 Geometry of Piezoelectric Pump

Figure 1 depicts the geometric structure of the piezoelectric pump. The micropump comprises a piezoelectric wafer, a metal substrate, a pump chamber, inlet and outlet channels, and check valves. The piezoelectric wafer is bonded to the metal substrate, forming the piezoelectric transducer. The one-way check valves are designed to control the unidirectional flow of fluid, functioning as fluid diodes to increase the output flow. The operational principle of the piezoelectric micropump utilizes the inverse piezoelectric effect, wherein the piezoelectric material converts electrical energy into mechanical energy for fluid transportation. The mechanism of the check valves relies on the application of an alternating voltage to a piezoelectric

Table 1 Geometric parameters of the piezoelectric micropump

Geometric parameter	Initial diameter/length	Initial thickness/height
Inlet/outlet	2 mm	/
Piezoelectric chip	20 mm	0.3 mm
Copper baseplate	30 mm	0.3 mm
Check valve	4 mm	0.2 mm
Pump chamber	30 mm	0.3 mm

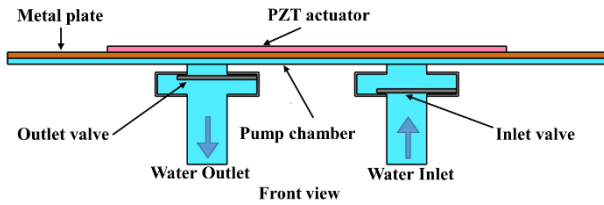


Fig. 1 Geometric structure of the piezoelectric pump

element, which causes the element to deflect. This deflection produces alternating pressure waves that are transmitted through the fluid, thereby modulating the function of cantilever beam valves. During the pumping cycle, as the piezoelectric actuator moves upward, fluid is drawn in, and the inlet valve opens upward to permit entry. Simultaneously, the outlet valve remains fully closed to prevent fluid from re-entering the micropump from the outlet channel. When the piezoelectric actuator moves downward, the outlet valve opens downward, enabling fluid to be pumped out, whereas the inlet valve remains fully closed, preventing backflow and preventing fluid from flowing out through the inlet channel.

2.2 Geometric Modeling of Piezoelectric Micropumps

Table 1 presents the parameters of the three-dimensional simulation model for the piezoelectric pump. The simplified three-dimensional model includes key components such as a piezoelectric transducer and check valves. The bonding layer between the copper substrate and the silver (Ag) electrode is disregarded because of its relatively negligible thickness compared with that of the other structural components.

Compared with 2D models, simulations based on the 3D model (Fig. 2(a)) offer significantly greater computational precision and accuracy compared to 2D

models. However, 3D model simulations require substantial computational resources and time. Therefore, this study employs a 3D axisymmetric simplification to reduce the simulation structure (Fig. 2(b)). Leveraging the inherent symmetry of the model significantly reduces the computational time without compromising the simulation accuracy. The mesh comprises 429,800 elements, and the transient calculation requires approximately 97 hours to compute two complete cycles.

2.3 Mesh Setting

The piezoelectric micropump model is discretized into tetrahedral, pyramidal, prismatic, triangular, and quadrilateral mesh elements. In this study, as shown in Fig. 3(a), the geometric model is divided into a total of 429,800 mesh elements. Local mesh refinement near the check valve walls is essential for accurately capturing the fluid–structure interaction characteristics. This refinement is critical for determining the valve opening dynamics and accurately calculating the pumping flow rates at both the inlet and outlet. In this model, check valves need to frequently open and close, requiring a dynamically adaptive fluid domain mesh to simulate these interactions accurately. The initial deformation of the check valves is set to zero, with the mesh velocity near the valves adjusting according to the valve deflection. As the inflow velocity increases and the valve opening increases, the mesh velocity increases accordingly, and the frequency of mesh redivision increases. In the bidirectional fluid–structure interaction (Fig. 3(b)), the moving mesh adapts to the deformation of the check valve. To ensure subsequent moving mesh redivision without generating new elements, the model assumes that the check valve is completely closed when the distance between the valve surface and the channel wall is less than 5×10^{-6} m.

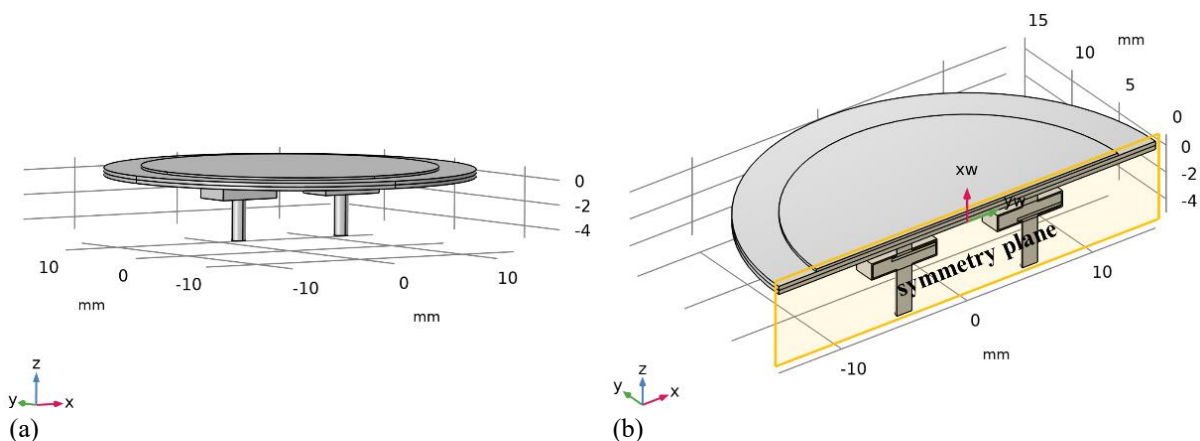


Fig. 2 Geometric model of a piezoelectric micropump

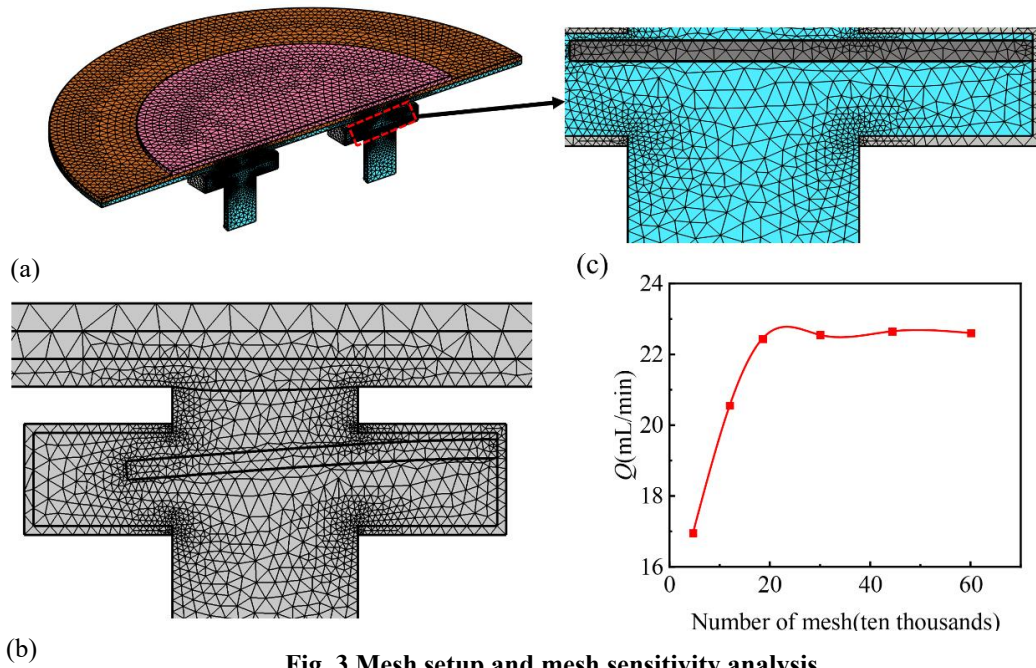


Fig. 3 Mesh setup and mesh sensitivity analysis

This study performed a mesh sensitivity analysis on the mesh structure employed in the simulation. The output flow rate was subjected to multiple simulations, each utilizing varying numbers of mesh elements, to identify and quantify variations in the convergence behavior of the solution. Six separate simulations were conducted using varying numbers of mesh elements to assess the effect of the mesh density on the model's accuracy. The mesh sensitivity analysis reveals how the micropump's maximum output varies with the number of mesh elements (Fig. 3(c)). The analysis indicates that when the mesh element count exceeds 200,000, the impact on the flow rate becomes negligible. Therefore, for optimal accuracy, this study employs 429,800 mesh elements for the mesh division of the model.

2.4 Control Equations

The fundamental governing equations for the model exceeds the momentum, energy, and continuity equations. These equations form the basis for numerical simulations and analysis. The following sections will elaborate on governing equations pertaining to the solid, fluid, and electrostatic domains.

2.4.1 Fluid Domain

Distilled water is utilized in the micropump to mitigate the risk of cavitation within the chamber. Cavitation, which occurs when dissolved gases in a fluid are released due to a pressure drop during high-velocity flow, can be detrimental to pump performance. Consequently, the fluid domain is modeled as an incompressible fluid. The continuity and momentum equations are presented below (Takaddus & Chandy, 2018)

$$\nabla \cdot u_{\text{fluid}} = 0 \quad (1)$$

$$\begin{aligned} & \rho \frac{\partial u_{\text{fluid}}}{\partial t} + \rho(u_{\text{fluid}} \cdot \nabla)u_{\text{fluid}} \\ & = \nabla \cdot [-pI + \mu(\nabla u_{\text{fluid}} + (\nabla u_{\text{fluid}})^T)] + F \end{aligned} \quad (2)$$

In these equations, u represents the fluid velocity, ρ represents the density, p represents the pressure, μ represents the dynamic viscosity, and F represents the external force.

2.4.2 Solid Domain

The solid mechanics interface encompasses linear elastic materials, fixed constraints, contact conditions, and piezoelectric materials. Linear elastic materials are assumed to be isotropic. The local equilibrium of the solid in transient analyses, which is essential for capturing dynamic responses, is represented by the following equation (Takaddus & Chandy, 2018):

$$\rho \frac{\partial^2 u_{\text{solid}}}{\partial t^2} = \nabla \cdot (FS)^T + F_V \quad (3)$$

In this equation, u represents the solid velocity, ρ represents the solid density, F_V represents the body force, and S represents the Piola-Kirchhoff stress. The deformation gradient F , a crucial quantity that describes the deformation of a solid, is defined by the following equation:

$$F = I + \nabla u_{\text{solid}} \quad (4)$$

Here, I denotes the identity tensor. The deformation gradient F encapsulates complete information about the local rotation and deformation of the material. The Lagrangian strain tensor ε is defined by the following equation:

$$\varepsilon = \frac{1}{2} [(\nabla u_{\text{solid}})^T + \nabla u_{\text{solid}} + (\nabla u_{\text{solid}})^T \nabla u_{\text{solid}}] \quad (5)$$

Here, T denotes the transpose of the term ∇u_{solid} .

2.4.3 Electrostatic Domain

An applied driving voltage on the surface of the piezoelectric material induces deformation, creating a pressure difference that drives the fluid. Additionally, the output force acts as a system excitation. The electrostatic and solid domains are coupled through electrostatic–structural multiphysics interactions, which are crucial for accurately modeling the behavior of the piezoelectric micropump. The electrostatic behavior is defined by the following equation:

$$\nabla \cdot D = \rho_v \quad (6)$$

Here, $\nabla \cdot D$ represents the divergence of the electric displacement field. ρ_v is the volume charge density. The electric potential is defined by the following equation:

$$E = -\nabla V \quad (7)$$

Here, E is the electrostatic field, and V is the electric potential.

2.4.4 Fluid–Solid Interaction

In addition to the fluid flow and structural mechanics interfaces within the fluid and solid domains respectively, the fluid–solid interaction method incorporates a multiphysics interface. The former is defined in the moving mesh (spatial coordinate system), and the moving mesh is an important component in fluid–structure interactions (FSIs). Its role is to dynamically adjust the fluid domain mesh in response to changes in the deformation of the solid. The moving mesh is typically implemented using the arbitrary Lagrangian–Eulerian (ALE) method, whereas the latter is defined in the material coordinate system. Typically, when the solid structure contacts the flowing fluid, the fluid exerts pressure and viscous forces on the boundary of the structure, causing deformation. Conversely, the deformed solid structure acts as a moving boundary for the flowing fluid, altering the flow field. In this study, the authors employed a bidirectional fluid–solid interaction method to calculate the flow within a piezoelectric micropump. The FSI interface provides the coupling between the fluid and the solid, transmitting fluid forces (such as pressure and shear forces) to the solid through boundary conditions and feeding back the displacement and deformation of the solid to the fluid. This process was achieved by transferring displacement data, induced by pressure fluctuations in the piezoelectric actuator, to the fluid domain. Simultaneously, the force data from the fluid domain were relayed back to the piezoelectric actuator and check valve, thereby accurately simulating the fluid–structure interaction (Singh et al., 2015). The fluid–solid interaction equations are provided as follows:

$$F_A = \left[-\rho I + \mu(\nabla u_{\text{fluid}} + (\nabla u_{\text{fluid}})^T) \right] \cdot n \quad (8)$$

$$u_{tr} = \frac{\partial u_{\text{solid}}}{\partial t} \quad (9)$$

Here, F_A represents the total force exerted by fluid on the fluid–solid boundary, n is the outward normal

direction, and u_{tr} is the rate of change in the solid displacement.

2.5 Boundary Conditions

In the setting of the piezoelectric actuator, the edges are fixed, ensuring that displacement is restricted in all directions. The piezoelectric sheet and metal substrate are bonded together, resulting in no relative displacement. In the fluid domain, both the inlet and outlet boundary conditions are set to atmospheric pressure. The inlet/outlet further constrains the velocity directions of the inflow and outflow to be perpendicular to their respective cross-sections. In the structural domain, the right end of the cantilever valve (the side in contact with the pump chamber) is fixed with a boundary condition of "zero displacement," indicating that there is no relative motion between the valve and the chamber at that interface. The left end of the cantilever valve is left free, which allows the valve to open and close during the pumping process. These conditions ensure precise control over the interactions within the piezoelectric micropump model, facilitating accurate simulations and analyses.

3. SIMULATION STUDY

3.1 Piezoelectric Actuator

The three-dimensional model of the micropump incorporates a single-layer piezoelectric actuator, with the geometric dimensions and material specifications detailed in Table 2. The actuator is driven by an electric field, which induces periodic deformations. These deformations cyclically alter the pump chamber volume. The check valve responds to this fluid movement by opening and closing, thus ensuring unidirectional fluid flow. The piezoelectric actuator is modeled within a material coordinate system, where the mesh deformation aligns with the material's intrinsic deformation, in contrast with the dynamic mesh changes observed in the bidirectional fluid–solid interaction domain. The bottom surface of the piezoelectric actuator is designated as the ground terminal, and the driving voltage is defined by the following equation (Singh et al., 2015):

$$V_0 = V_i(\sin 2\pi ft) \quad (10)$$

Here, t denotes time (s), and f denotes frequency (Hz). To enhance the convergence of the model, the terminal conditions for the electric field in the simulation are defined by the following equation:

$$V_0 = V_i(\sin 2\pi ft)rm \quad (11)$$

Here, rm denotes a ramp function, enabling the applied electric field load to gradually increase to the target value during model initialization. This approach ensures a smooth start-up phase for the simulation, promoting stability and accuracy in the model's convergence.

3.2 Flow State Determination

A crucial criterion for determining the flow regime within the pump chamber—whether laminar or turbulent—is the Reynolds number. According to the

Table 2 Specifications of Piezoelectric Transducer Materials

Elements	Materials	Density (kg/m ³)	Modulus of Elasticity (GPa)	Poisson's Ratio
Piezoelectric element	PZT-5H	7500	63	0.32
Substrate	Copper	8960	200	0.35
Pump chamber	PMMA	1190	3.16	0.32
cantilever-valve	PDMS	1030	0.87	0.5

definition of turbulence, the Reynolds number has a critical value range (transition state $Re = 2320\sim 4000$). If the Re surpasses this critical range, the flow transitions to a turbulent state; if it remains below this range, the flow is laminar. The Re is computed using the following equation,

$$Re = \frac{\rho UL}{\mu} \tag{12}$$

Here, $\rho=996 \text{ kg/m}^3$, $\mu=7.98 \times 10^{-4} \text{ kg/m}\cdot\text{s}$, and $L=0.002 \text{ m}$. The maximum fluid velocity in the fluid domain reaches $13.79 \times 10^{-2} \text{ m/s}$; thus, $Re=344.23 < 2320$. Consequently, on the basis of the calculated Reynolds number and the defined critical value range, the flow is laminar.

3.3 Model Solution

In this model, the flow domain is considered incompressible and laminar, whereas the effects of gravity are neglected. To increase solution stability, an additional subnode for self-consistent stabilization was incorporated at the laminar flow interface. Streamline diffusion was incorporated into the Navier–Stokes equations to describe momentum transfer in the fluid, and a dynamic subgrid time scale was employed to prevent oscillations in the solution. The precision of the solver in resolving the bidirectional fluid–solid coupling and arbitrary Lagrangian–Eulerian equations is critical to the model solution. Therefore, a self-consistent stabilization method is employed to ensure high spatial resolution for oscillatory problems. For transient problems, the accuracy of the transient solver is governed by relative and absolute tolerance limits, which are set at 0.005 and 0.05, respectively. In the laminar domain, fluid velocity and pressure are resolved using linear shape functions; the displacement field in solid mechanics is discretized using quadratic Lagrange elements; and the potential in the electrostatic domain is discretized using quadratic elements.

3.4 Model Validation

The simulation model described above was validated using experimental data from [Vante and Kanish \(2024\)](#). Abhijeet B. Vante and colleagues conducted experimental studies on the impact of various frequencies and voltages on the output of a micropump. The driving voltages for different test conditions were set at 100 V, 150 V, 200 V and 250V, with driving frequencies of 10 Hz, 20 Hz, 30 Hz, 40 Hz and 50 Hz for each voltage. To efficiently validate the accuracy of the simulation model efficiently, only 30 Hz and 40 Hz were selected as sample data for simulation validation. The results are depicted in Fig. 4. At a driving voltage of 100 V, the numerical simulations closely align with the experimental findings. However, as the voltage increases, the simulated output flow rate

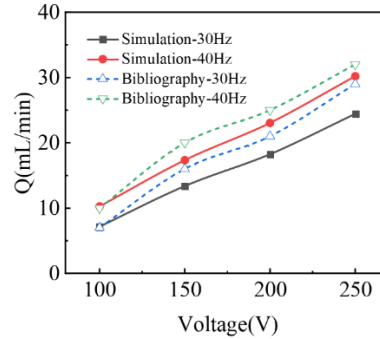


Fig. 4 Validation of the simulation model

becomes slightly lower than the experimental output. Specifically, the maximum deviation observed was 15.51%, and the root mean square error (RMSE) between the simulated results and experimental data was 2.51, which falls within the acceptable range, thereby validating the accuracy of the simulation model.

4. RESULTS AND DISCUSSION

4.1 Analysis of Operating Characteristics

During the working cycle, the piezoelectric actuator undergoes a periodic deformation process consisting of upward deformation, restoration, downward deformation, and subsequent restoration, corresponding to fluctuations in the driving voltage. Figure 5(a) shows the maximum displacement of the piezoelectric element throughout the entire micropump cycle as the driving voltage varies. The simulated operating conditions for the driving voltage and frequency are set at 200 Vp and 40 Hz, respectively, which are the parameters chosen to highlight the actuator's response under typical operating conditions. At the peak driving voltage, the geometric center of the piezoelectric actuator achieves a maximum deformation displacement of 21.6 μm , which is indicative of the actuator's sensitivity to voltage changes. Figure 5(b) depicts the deformation of the entire piezoelectric actuator at specific time points, where the deformation surface resembles an "umbrella" shape. This distinctive deformation pattern is important, as it impacts the efficiency of fluid displacement, which is consistent with findings from previous studies on piezoelectric actuator behavior

The micropump structure incorporates two check valves. Figure 6(a) shows the fluid field distribution within the fluid domain of the micropump during both the suction and discharge phases. For the left subfigure of Fig. 6(a), the color bar represents the logarithmic normalization of the velocity, specifically

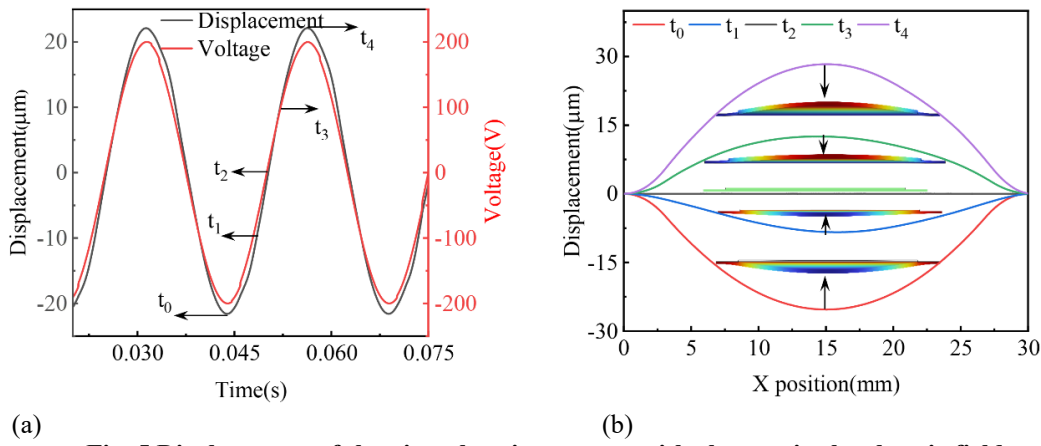


Fig. 5 Displacement of the piezoelectric actuator with changes in the electric field

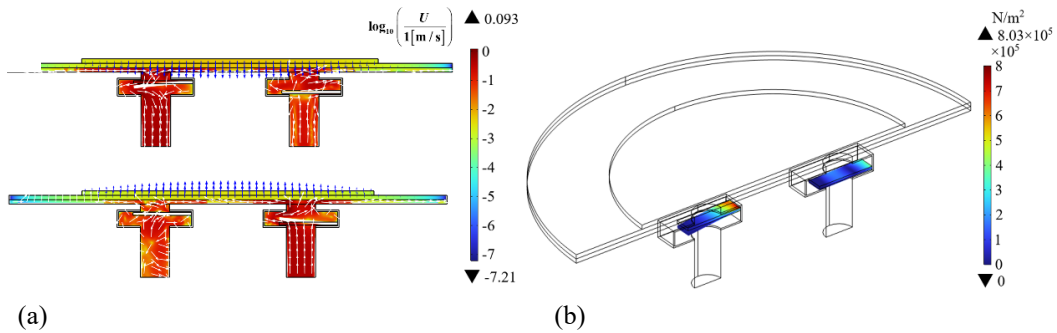


Fig. 6 Flow field distribution and valve stress distribution

$\log_{10}\left(\frac{U}{1[m/s]}\right)$, where U denotes the velocity field, the

flow field is indicated by white arrows, and the displacement velocity of the piezoelectric actuator is shown with blue arrows. The periodic up-and-down motion of the piezoelectric actuator causes cyclical changes in the pump chamber volume, resulting in fluid flowing in or out due to the driving pressure differential. The pressure exerted by the fluid acts on the check valve, causing it to alternate between open and closed states according to the prevailing operating conditions. Conversely, the material characteristics of the check valve generate a force upon deformation, which acts on the surrounding fluid. Therefore, the valve opening (the maximum deflection from its initial position for a cantilever valve) also influences the micropump's output characteristics. In the design process of the check valve, understanding the operational forces is crucial, as exceeding the strength limit poses a failure risk. Figure 6(b) depicts the effective stress experienced by the check valve. One criterion for evaluating check valve failure is whether the von Mises stress exceeds the material's limit. Under the selected simulated conditions, the maximum stress at the root of the check valve reaches 803 kPa. These findings indicate that the performance of the check valve is critical for the overall efficiency of the micropump.

The following analysis delves deeper into the fluid-structure interaction characteristics within the piezoelectric micropump. Specifically, Fig. 7 presents the temporal variations in key parameters over two stable

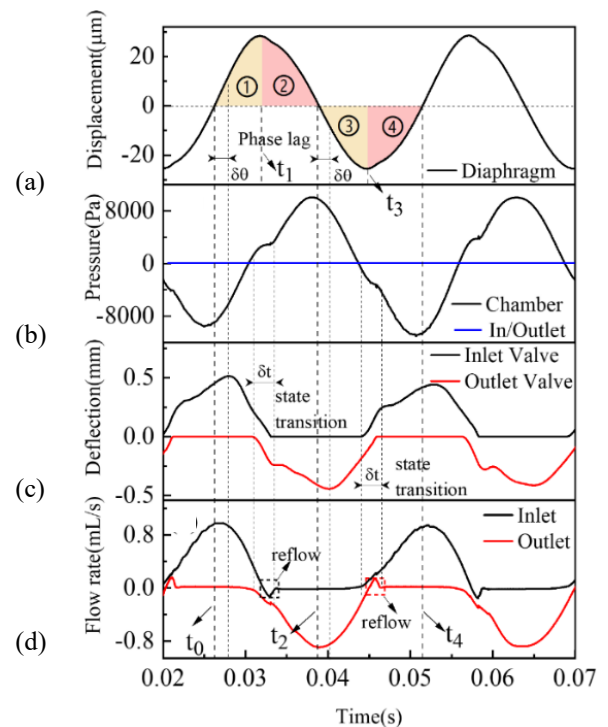


Fig. 7 Fluid-structure interactions in micropumps

cycle periods: the instantaneous fluid flow rate at the inlet/outlet (see Fig. 7(d)), the opening states of the inlet/outlet check valves (see Fig. 7(c)), the average gauge pressure within the micropump (see Fig. 7(b)), and the displacement of the piezoelectric actuator (see Fig. 7(a)).

For analysis of the working process of the micropump, the periods ① to ④ (i.e., one stable cycle period) are examined. The subsequent periods are repetitions of this cycle and are therefore not described further.

A cycle period is divided into four stages. In the first quarter period ① from t_0 to t_1 , which marks the start of the cycle (i.e., when the piezoelectric actuator begins to move upward from the zero displacement position), the piezoelectric actuator moves upward from the initial position state to the point of maximum positive displacement, driven by a sinusoidal alternating voltage. Liquid is drawn into the micropump from the inlet channel, causing the pressure in the chamber to stop decreasing and gradually increasing back to 0 Pa. As the pressure difference between the inlet channel and the chamber decreases, the flow dynamics are altered accordingly. The opening of the inlet check valve and the instantaneous volumetric flow rate of the incoming fluid both gradually decrease, whereas the outlet check valve remains closed, keeping the instantaneous flow rate of the outlet liquid at 0 mL/s.

In the second quarter period ②, from t_1 to t_2 , as the piezoelectric actuator returns to the zero displacement position, the pump chamber volume decreases, resulting in an increase in pressure within the pump chamber. Consequently, as the pressure difference between the outlet channel and the chamber increases, the outlet cantilever beam valve opens wider, allowing the instantaneous volumetric flow rate of the outlet liquid to increase. During this phase, the inlet cantilever beam valve remains closed, maintaining the volumetric flow rate of the inlet liquid at 0 mL/s.

The third quarter period ③, from t_2 to t_3 and the fourth quarter period ④, from t_3 to t_4 exhibit motion patterns similar to those of the first and second quarter periods but with opposite trends. At times t_1 , t_2 , t_3 , and t_4 , the cloud diagrams in Fig. 8 illustrate the pressure distribution within the micropump, the deformation of the piezoelectric actuator, and the openings of the check valves.

Notably, when the piezoelectric actuator reaches the zero displacement moment (specifically at the junction of the second and third quarter periods), the deflection of the check valve and the instantaneous volumetric flow rate of the outlet liquid do not reach their maximum values. These maximum values occur at a phase difference (the time shift between the oscillations of the piezoelectric actuator and the valve's movement) of $\delta\theta(\frac{4}{25}\pi)$ from the

zero displacement moment of the piezoelectric actuator. This delay occurs because the pressure wave generated by the volume change within the chamber requires time to propagate through the liquid, causing actuation of the check valve to lag behind the motion of the piezoelectric actuator. Moreover, if the driving frequency increases beyond a certain threshold, the output of the micropump decreases to zero because of the time lag in the actuation of the check valve.

Second, when the piezoelectric actuator returns to the

zero displacement position (at the junctions of the first/second and third/fourth quarter periods), the inlet and outlet check valves change their states between open and closed. The rate of change in pressure within the pump chamber decelerates (see Fig. 7(b)) as the instantaneous volumetric flow rates of the inlet and outlet fluids approach zero. As illustrated in Fig. 7(c), during this δt interval, the outlet check valve begins to actuate before the inlet check valve is fully closed or opened. Both the outlet and inlet check valves exhibit a lag in transitioning from open to closed compared with the transition from closed to open. This results in a slight backflow at the micropump's inlet and outlet, which is negligible over the entire cycle and has a minimal impact on the micropump's output flow rate. Simulations of the optimized piezoelectric pump reveal that the phase lag induced by the mechanical inertia of the valve causes a transient backflow, accounting for approximately 1.66% of the total output during each valve cycle. This transient backflow contributes to a corresponding reduction in the overall pumping efficiency. Without backflow, the optimized piezoelectric micropump is capable of achieving an output flow rate of 34.58 mL/min. Before optimization, the transient backflow in the piezoelectric micropump constituted approximately 5.11% of the total output flow. This finding indicates a substantial improvement in mitigating backflow after optimization. We performed a comparative analysis of backflow losses by reviewing the relevant literature (Jenke et al., 2018) and comparing these losses with typical flow losses observed in similar piezoelectric micropumps. The literature reports that in shallow pump chambers, fluid viscous losses can reduce the output flow by 23% to 43%. Valve-related flow reductions range from 6.2% to 12.4%, and under conditions of stable cavitation, where bubble formation occurs, the output flow can decrease to as low as 65% of the original flow. In the present study, the backflow losses attributed to the mechanical inertia of the valve range from 1.66% to 5.11%. Compared with other flow loss mechanisms, the impact of the valve is relatively minor. In our investigation of cavitation losses within the micropump, we note that many researchers use the minimum system pressure as a criterion to determine the onset of cavitation. During the operation of the micropump, the pressure at the start of the suction phase is the lowest, and cavitation will occur whenever this pressure falls below the saturated vapor pressure. Conversely, cavitation is suppressed when the pressure remains sufficiently high above the saturated vapor pressure. For the micropump model analyzed in this study, we investigated pressure variations within the pump chamber over two operational cycles. The minimum pressure during the suction phase was -10.8 kPa (absolute pressure of 90.5 kPa), whereas the saturated vapor pressure of water at 25 °C was 3.17 kPa. Given these values, we conclude that cavitation is effectively suppressed in our system. As a result, we assume that cavitation losses do not occur in our simulations. However, we acknowledge that real cavitation losses could be quantified through experimental measurements, which would offer more accurate data for validation. With respect to the influence of the damping of the piezoelectric actuator on the micropump performance, damping plays a

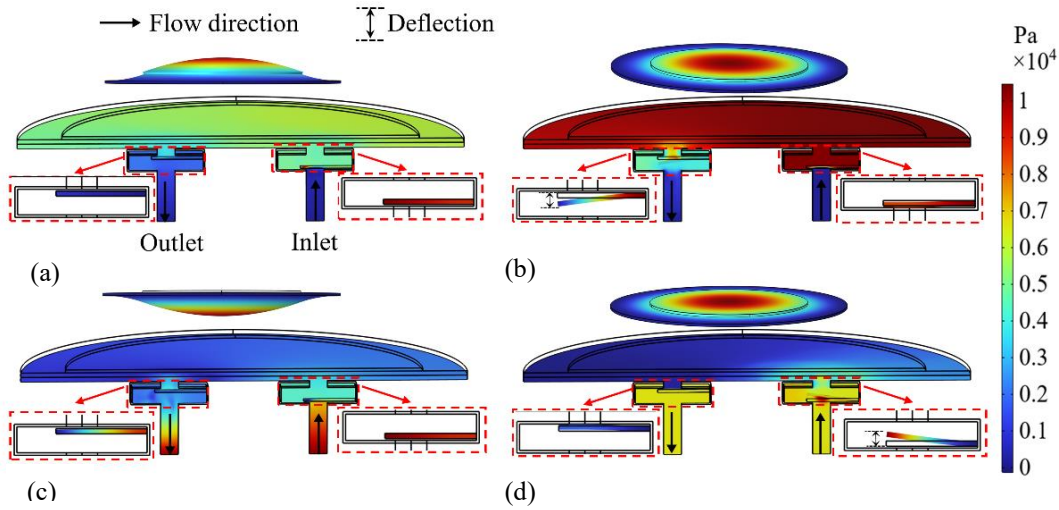


Fig. 8 Pressure distribution, piezoelectric actuator displacement, and check valve opening in the micropump at times t_1 , t_2 , t_3 and t_4

critical role in determining the output flow. In shallow chamber micropumps, damping increases cubically as the distance between the piezoelectric actuator and the chamber boundary decreases. In our study, we explored the effect of the pump chamber height on the output flow at 200 V and 40 Hz. The simulation results indicate that when the chamber height exceeds 0.3 mm, the output flow stabilizes. This finding suggests that the damping effect of the piezoelectric actuator on the output flow stabilizes at these chamber heights. However, when the chamber height is reduced to 0.2 mm, a substantial decrease in the output flow is observed. After excluding valve losses, we attributed the 5.53% flow loss to the increased damping caused by the reduced chamber height.

The volumetric flow rate $Q_{in/out}$ of the micropump is given by the following equation (Ni et al., 2023):

$$Q_{in/out} = \frac{\int_{t_0}^{t_1} \pi r^2 v dt}{t_1 - t_0} \text{ (mL/min)} \quad (13)$$

Here, v denotes the surface fluid velocity at the inlet/outlet, and r is the radius of the inlet or outlet pipe.

The cumulative inlet fluid intake, V_{in} , and the cumulative outlet fluid output, V_{out} , of the piezoelectric micropump can be determined by integrating the volumetric flow rate over time, as given by the following equations:

$$V_{in/out} = \int_{t_0}^{t_1} Q_{in/out} dt \text{ (\mu L)} \quad (14)$$

Figure 9 shows the cumulative flow rates of the piezoelectric micropump over two stable cycles, with the output flow rate being approximately 22.54 mL/min.

4.2 Optimization of Piezoelectric Micropump Structure

In this section, we present a detailed analysis of how the driving voltage, frequency, piezoelectric plate diameter, thickness, inlet/outlet diameter, and pump chamber height influence the micropump output flow. While the impact of each parameter on the micropump's

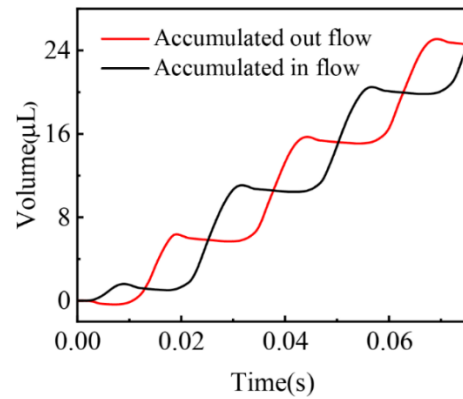


Fig. 9 Cumulative flow rates of the micropump

output flow is studied, the other parameters remain constant at their initial values. Figures 10(a) and 10(b) show the micropump output with the driving voltage and frequency as variables. With a constant frequency, the micropump's output flow increases with the driving voltage because of the positive correlation between the piezoelectric actuator's amplitude and the driving voltage. Conversely, with a constant voltage, the growth rate of the micropump's output flow gradually decreases as the frequency increases. This finding is because an increase in the driving frequency results in an increased lag of the check valve, causing more fluid backflow and reduced output performance. Therefore, the piezoelectric micropump has an optimal operating frequency.

The influences of the PZT radius and thickness on the micropump output performance are illustrated in Figs. 10(c) and 10(d). As the PZT radius increases from 6 mm to 12 mm, the micropump output flow initially rises from 6.72 mL/min to 25.44 mL/min. However, when the PZT radius further increases to 14 mm, the micropump output flow decreases to 19.96 mL/min. For a PZT radius of less than 12 mm, a smaller radius results in a lower output flow due to the reduced changeable volume of the chamber, leading to a lower pressure difference generated by the volume change and diminished fluid intake or discharge

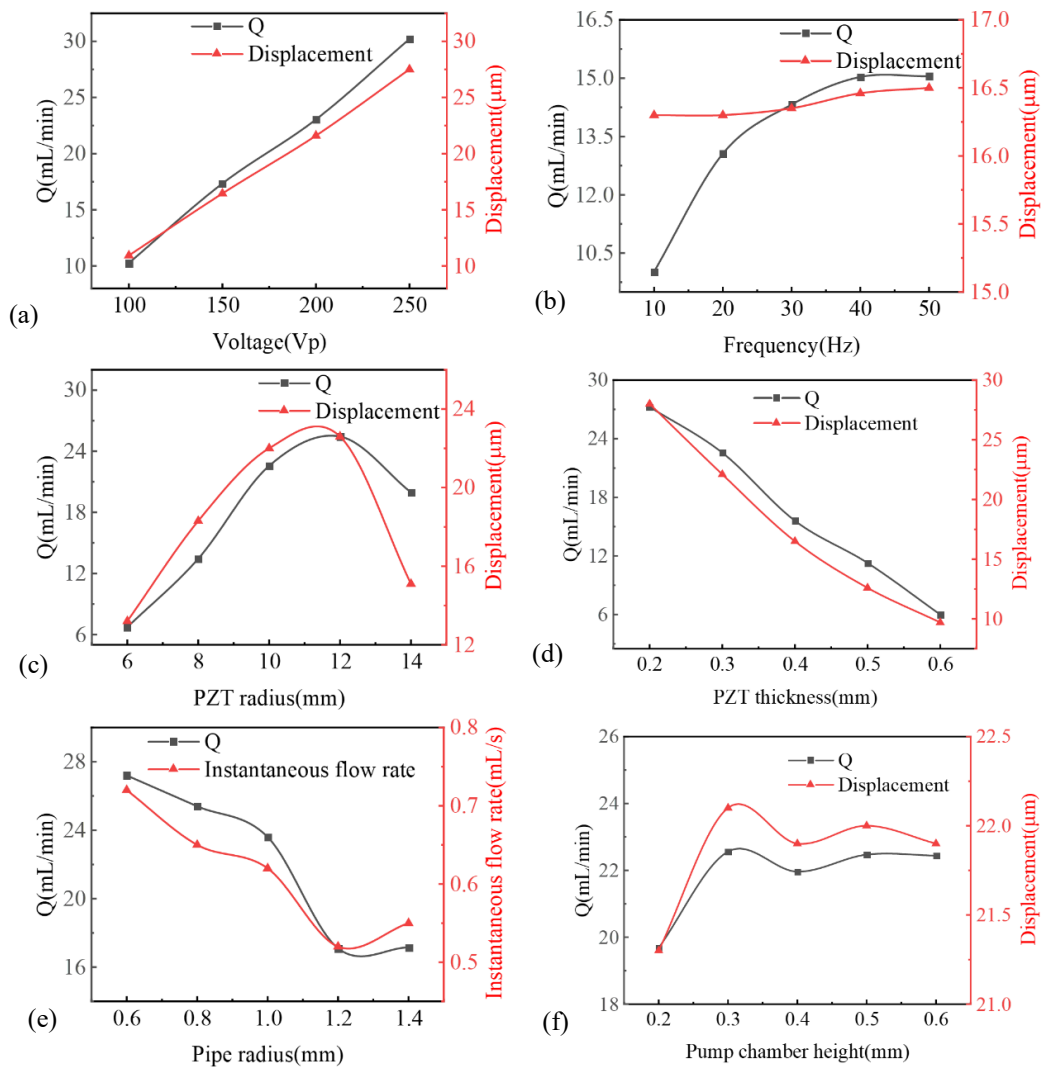


Fig. 10 Impact of different structural parameters on the micropump's output performance

capability. When the PZT radius exceeds 12 mm, the micropump output decreases. This change occurs because the deformation of the piezoelectric actuator has not reached its maximum potential under these conditions. Although the theoretical variable volume range increases, it does not reach the variable limit. Furthermore, the PZT diameter is constrained by the substrate diameter, and optimal micropump performance is achieved only when the ratio between these diameters is appropriate. As the PZT thickness varies from 0.2 mm to 0.6 mm, the output flow varies from 27.24 mL/min to 6 mL/min. This reduction occurs because, with increasing PZT thickness under a constant voltage, the maximum piezoelectric actuator deformation gradually decreases, leading to a smaller change in the pump chamber volume. Essentially, this effect weakens the electric field intensity on the upper surface of the PZT.

Additionally, the impact of the pipe radius on the output performance of the micropump was investigated, as illustrated in Fig. 10(e). When the pipe radius varies from 0.6 mm to 1.4 mm, the output varies from 27.2 mL/min to 17.1 mL/min. This phenomenon occurs because, with a larger pipe radius, the efficiency of fluid intake or discharge decreases, and the backflow increases during the check valve's open/close state transition,

leading to reduced micropump performance. Figure 10(f) illustrates the influence of chamber height on the micropump's output performance. When the chamber height exceeds 0.3 mm, the output remains constant at 22.47 mL/min. However, when the chamber height decreases to 0.2 mm, the output decreases to 19.68 mL/min. This reduction in pumping flow is attributed to the lower chamber height, which impedes movement of the piezoelectric actuator, thereby reducing its maximum positive displacement.

This study investigated the impact of the applied driving voltage and frequency on the operating characteristics of a piezoelectric micropump, focusing on the variations in the maximum opening of the check valve and associated backflow losses. The applied voltage varied from 100 V to 250 V, while the frequency ranged from 10 Hz to 50 Hz (Fig. 11). The results demonstrate that both the applied voltage and frequency contribute to an increase in the maximum opening of the check valve. Additionally, the backflow loss decreases as the voltage increases. Specifically, when the frequency is less than 40 Hz, the backflow loss decreases with increasing frequency. However, beyond a voltage of 100 V and a frequency of 40 Hz, the backflow loss begins to increase.

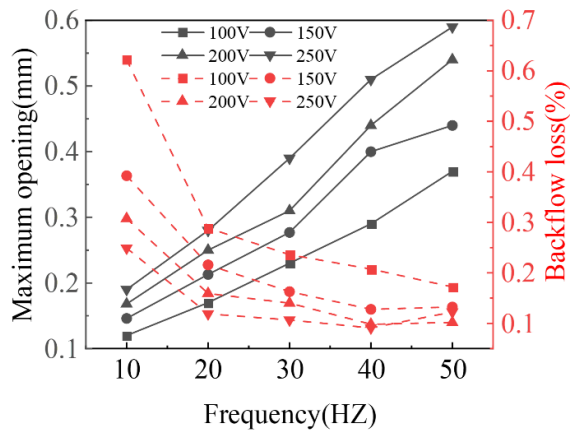


Fig. 11 Backflow losses and maximum valve opening of the micropump under different applied driving voltages and frequencies

This behavior can be explained by the positive correlation between the applied driving voltage and the maximum deformation displacement of the piezoelectric actuator (Fig. 10(a)). As the actuator deforms more, the pressure within the pump chamber increases accordingly. This pressure is transmitted to the check valve via the fluid, leading to an increase in the valve's maximum opening and, in turn, improving the suction and pumping efficiency of the micropump. As a result, the output flow of the micropump increases with increasing applied voltage. Although the external driving frequency has a relatively minor effect on the maximum deformation displacement of the piezoelectric actuator (Fig.10(b)), increasing the frequency still results in a higher pressure within the pump chamber. This finding is because, as the frequency increases, the driving cycle shortens, causing the actuator to deform more frequently and, therefore, imparting greater kinetic energy to the fluid per unit time. The compression and expansion of the fluid occur more frequently, and at higher frequencies, the inertial effects of the fluid within the pump chamber become more important. This effect impedes the ability of the fluid pressure to stabilize at a new equilibrium. As a result, the pressure within the pump chamber becomes relatively high. For example, at a voltage of 200 V, when the frequency increases from 10 Hz to 50 Hz, the maximum pressure inside the chamber increases from 0.77 kPa to 8 kPa, leading to an increase in the maximum opening of the check valve. However, owing to the hysteresis behavior of the check valve, an increase in frequency exacerbates backflow loss. This effect is particularly pronounced at 50 Hz, where the backflow loss exceeds that observed at 40 Hz.

Moreover, the study indicates that under low voltage conditions, backflow loss represents a greater proportion of the total output flow, although its absolute value is lower than that of higher voltages. This finding is because, at low voltage, the piezoelectric actuator's amplitude is small, resulting in weaker output performance from the micropump, with the applied voltage being the primary factor influencing the micropump's output capacity. As the frequency increases, the hysteresis behavior of the

check valve becomes more pronounced, amplifying the impact of the loss of the valve on the backflow loss.

Additionally, this study examines the impact of the applied driving voltage and frequency on the structural dimensions of the micropump, with the corresponding simulation results shown in Fig. 12. The bar charts in Fig. 12 depict the variations in the micropump's output flow under different conditions. Figures 12(a) and 12(b) illustrate the effects of the applied voltage and frequency on the dimensions of the check valve. The results indicate that within the studied voltage and frequency range, the check valve length has a minimal effect on the micropump output flow. Although increasing the length of the check valve leads to a larger maximum opening, it simultaneously complicates the fluid flow dynamics around the valve leaf. In contrast, the thickness of the check valve is more sensitive to increases in both voltage and frequency. For example, at a voltage of 200 V and a frequency of 40 Hz, a 0.1 mm increase in the check valve thickness (from 0.2 mm to 0.3 mm) leads to a considerable decrease in the micropump's output flow. This effect can be attributed to the reduction in the maximum opening of the check valve caused by the increased thickness.

Figures 12(c) and 12(d) illustrate the effects of the voltage and frequency on the dimensions of the piezoelectric actuator. The results indicate that the influence of voltage and frequency on the dimensions of the piezoelectric actuator is consistent across actuators of different sizes. Under conditions of 100 V, 40 Hz and 200 V, 20 Hz, the output flow of the micropump, driven by piezoelectric actuators of various sizes, remains virtually unchanged.

Figures 12(e) and 12(f) illustrate the effects of voltage and frequency on the pipe radius and pump chamber height. The study revealed that the micropump output flow decreases progressively as the pipe radius increases, with the effect being more pronounced under low-voltage and low-frequency conditions. This phenomenon occurs because, under low-voltage and low-frequency conditions, the pressure within the pump chamber decreases significantly as the pipe radius increases. This reduction in pressure diminishes the micropump's suction and pumping capability while simultaneously causing a substantial increase in backflow losses. In contrast, the influence of voltage and frequency on the pump chamber height is relatively negligible.

Figure 13 shows a comparison of the performance of the micropump before and after structural optimization. Table 3 shows a comparison of the size and performance of the piezoelectric micropump before and after optimization. The optimized micropump substantially improved the output performance. As depicted in Fig. 11(a), the instantaneous volumetric flow rate of the optimized micropump reaches 0.98 mL/s, representing a 46.27% increase compared with that before optimization. This increase is largely attributed to an increase in the maximum amplitude of the piezoelectric actuator, which increases by 28.05% to 28.3 μ m. A comparison of the cumulative output flow of the micropump before and after optimization is shown in Fig. 11(b), with the optimized output increasing from 54.54% to 34.02 mL/min. The

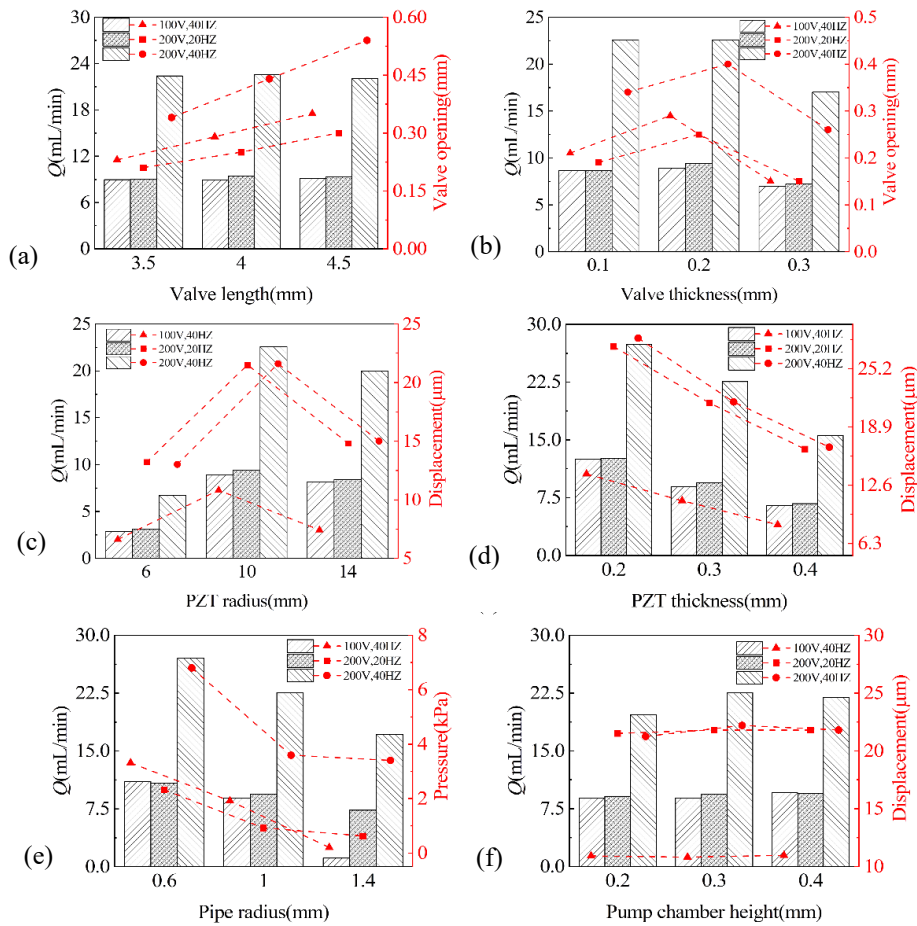


Fig. 12 Effects of varying the applied voltage and frequency on the performance of micropumps with different geometries

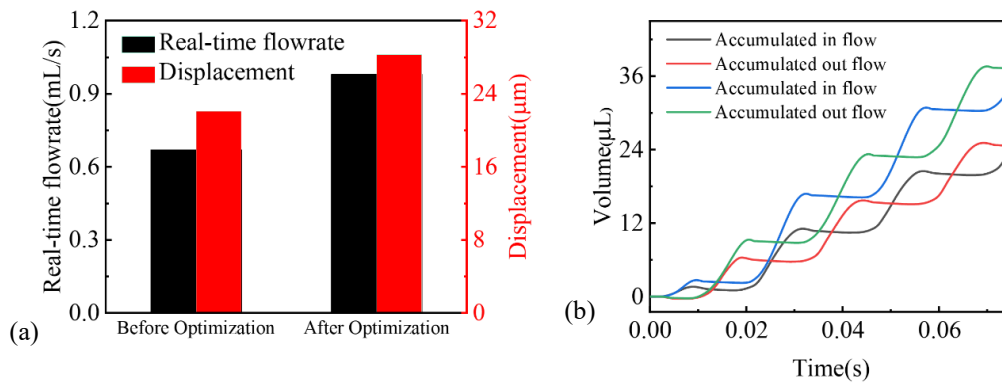


Fig. 13 Comparative analysis of the micropump performance metrics before and after optimization

Table 3 Performance metrics of the micropump before and after the optimization

Elements	Initial	Post-optimization
Real-time flowrate(mL/s)	0.67	0.98
Displacement(μm)	22.06	28.3
Output flow(mL/min)	22.02	34.02
Pipe radius(mm)	1	0.6
PZT radius(mm)	10	12
PZT thickness(mm)	0.3	0.2
Pump chamber height(mm)	0.3	0.3

optimized micropump achieves faster fluid intake and discharge rates, significantly increasing the efficiency. Crucially, the optimized micropump maintains nearly constant opening and closing times for check valves, thereby ensuring consistent operation. This consistency results in higher throughput during the same intake or discharge periods, enhancing the overall performance of the micropump.

5. OUTPUT-BACK PRESSURE CHARACTERISTICS

The back pressure within the fluid system of a

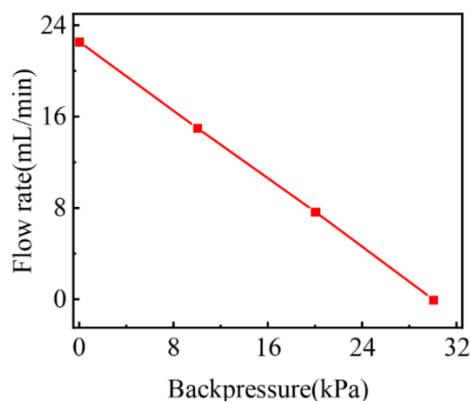


Fig. 14 Output-back pressure characteristics

micropump varies depending on its application scenario. When the back pressure changes, the micropump's output flow rate adjusts correspondingly. Consequently, determining the relationship between back pressure and output is essential for optimizing micropump performance across different applications. Figure 14 shows the micropump output flow characteristics under various back pressure conditions. As the back pressure exerted on the micropump increases, the output gradually decreases. This reduction occurs because increased back pressure introduces greater resistance to fluid movement, thereby diminishing the effective volumetric displacement. Under the conditions of a 200 V input voltage and a 40 Hz driving frequency, the micropump reaches a maximum output of 22.56 mL/min at 0 kPa back pressure. However, when the back pressure reaches 30 kPa, the output decreases to zero, indicating that the upper limit of the back pressure the micropump can handle. This finding suggests that for applications demanding high back pressure, the performance of the micropump may be constrained. Notably, as the applied back pressure increases from 0 kPa to 30 kPa, the relationship between the output pressure and back pressure remains linear, indicating consistent and predictable performance within this range.

6. CONCLUSION

This study presents the analysis, design, and structural optimization of a piezoelectric micropump incorporating passive check valves. A geometric model and a 3D simulation model of the cantilever valve micropump were developed, followed by a bidirectional fluid–solid coupling simulation to determine the micropump's operational characteristics. The numerical simulation model was validated against experimental data, confirming its reliability and accuracy in predicting pump behavior.

The results clearly demonstrate that under a sinusoidal alternating voltage, the piezoelectric actuator exhibits maximum deformation at its geometric center, following a sinusoidal pattern. This deformation induces synchronous oscillations in the pump chamber pressure, mirroring the sinusoidal fluctuations of the driving voltage. The valve's dynamic response adjusts to pressure fluctuations within the chamber; however, owing to the

mechanical inertia of the valve (the resistance of the mass of the valve to changes in motion), its opening lags behind the pressure wave propagation in the fluid, introducing a phase difference, $\delta\theta$. This delay in the valve response results in transient backflow during the state transition, which is a critical factor affecting the overall efficiency of the micropump. These findings highlight the importance of addressing the phase lag in valve dynamics to minimize backflow and optimize the performance of piezoelectric micropumps. The observed correlation between the actuator deformation, pressure oscillations, and valve response underscores the intricate interplay among the electrical, mechanical, and fluidic components of the system, providing essential insights for further structural optimization.

The parameters influencing the micropump output flow were subsequently analyzed and simulated. On the basis of these results, the optimal structure of the micropump was determined within the constraints of the overall geometric dimensions. Compared with the preoptimization design, the output of the optimized micropump increased by 54.54%, reaching 34.02 mL/min. Furthermore, the micropump output under various back pressures was studied. The results indicate that the micropump achieves its maximum output at 0 kPa back pressure, with a maximum operational back pressure of 30 kPa. Additionally, the output-back pressure characteristics of the micropump exhibit a linear relationship.

ACKNOWLEDGMENTS

This work was supported by National Natural Science Foundation of China (Grant No.52276054,92373118).

CONFLICT OF INTEREST

There are no conflicts of interest.

AUTHOR CONTRIBUTION

Y. F. Zhang: Software, Data Curation, Formal analysis, Writing - Original Draft, Visualization. **B. Zhou:** Conceptualization, Writing - Review & Editing. **Z. L. Deng:** Conceptualization, Methodology, Writing - Review & Editing, Funding acquisition.

REFERENCES

- Asadi Dereshgi, H., Yildiz, M. Z., & Parlak, N. (2020). Performance comparison of novel single and bi-diaphragm PZT based valveless micropumps. *Journal of Applied Fluid Mechanics*, 13(2), 401-412. <https://doi.org/10.29252/jafm.13.02.30347>
- Bayazidi, S., Mojaddam, M., & Mohseni, A. (2023). Performance optimization of nozzle-diffuser piezoelectric micropump with multiple vibrating membranes by design of experiment (DOE) method. *Journal of Applied Fluid Mechanics*, 16(7), 1356-1370. <https://doi.org/10.47176/jafm.16.07.1539>
- Bui, G. T., Wang, J. H., & Lin, J. L. (2017). Optimization of micropump performance utilizing a single

- membrane with an active check valve. *Micromachines*, 9(1), 1. <https://doi.org/10.3390/mi9010001>
- Bußmann, A., Leistner, H., Zhou, D., Wackerle, M., Congar, Y., Richter, M., & Hubbuch, J. (2021). Piezoelectric silicon micropump for drug delivery applications. *Applied Sciences*, 11(17), 8008. <https://doi.org/10.3390/app11178008>
- Carrozza, M. C., Croce, N., Magnani, B., & Dario, P. (1995). A piezoelectric-driven stereolithography-fabricated micropump. *Journal of Micromechanics and Microengineering*, 5(2), 177. <https://doi.org/10.1088/0960-1317/5/2/032>
- Cazorla, P. H., Fuchs, O., Cochet, M., Maubert, S., Le Rhun, G., Fouillet, Y., & Defay, E. (2016). A low voltage silicon micro-pump based on piezoelectric thin films. *Sensors and Actuators A: Physical*, 250, 35-39. <https://doi.org/10.1016/j.sna.2016.09.012>
- Cui, Q., Liu, C., & Zha, X. F. (2008). Simulation and optimization of a piezoelectric micropump for medical applications. *The International Journal of Advanced Manufacturing Technology*, 36, 516-524. <https://doi.org/10.1007/s00170-006-0867-x>
- Dau, V. T., & Dinh, T. X. (2015). Numerical study and experimental validation of a valveless piezoelectric air blower for fluidic applications. *Sensors and Actuators B: Chemical*, 221, 1077-1083. <https://doi.org/10.1016/j.snb.2015.07.041>
- Dong, J. S., Chen, W. H., Zeng, P., Liu, R. G., Shen, C., Liu, W. S., & Lin, B. S. (2017a). Design and experimental research on piezoelectric pump with triple vibrators. *Microsystem Technologies*, 23, 3019-3026. <https://doi.org/10.1007/s00542-016-3029-6>
- Dong, J. S., Liu, R. G., Liu, W. S., Chen, Q. Q., Yang, Y., Wu, Y., & Lin, B. S. (2017b). Design of a piezoelectric pump with dual vibrators. *Sensors and Actuators A: Physical*, 257, 165-172. <https://doi.org/10.1016/j.sna.2017.02.001>
- Gidde, R. R., Pawar, P. M., & Dhamgaye, V. P. (2020). Fully coupled modeling and design of a piezoelectric actuation based valveless micropump for drug delivery application. *Microsystem Technologies*, 26(2), 633-645. <https://doi.org/10.1007/s00542-019-04535-8>
- Jenke, C., Kager, S., Richter, M., & Kutter, C. (2018). Flow rate influencing effects of micropumps. *Sensors and Actuators A: Physical*, 276, 335-345. <https://doi.org/10.1016/j.sna.2018.04.025>
- Johari, J., & Majlis, B. Y. (2008, November). *Flow behaviour of fluid-structure interaction (FSI) system of piezoelectric actuated valveless micropump (PAVM)*. 2008 IEEE International Conference on Semiconductor Electronics (pp. 216-220). IEEE. <https://doi.org/10.1109/SMELEC.2008.4770311>
- Kaçar, A., Özer, M. B., & Taşcıoğlu, Y. (2020). A novel artificial pancreas: Energy efficient valveless piezoelectric actuated closed-loop insulin pump for T1DM. *Applied Sciences*, 10(15), 5294. <https://doi.org/10.3390/app10155294>
- Kang, J., & Auner, G. W. (2011). Simulation and verification of a piezoelectrically actuated diaphragm for check valve micropump design. *Sensors and Actuators A: Physical*, 167(2), 512-516. <https://doi.org/10.1016/j.sna.2011.01.012>
- Kaviani, S., Bahrami, M., Esfahani, A. M., & Parsi, B. (2014). A modeling and vibration analysis of a piezoelectric micro-pump diaphragm. *Comptes Rendus Mécanique*, 342(12), 692-699. <https://doi.org/10.1016/j.crme.2014.06.005>
- Lee, D. G., Or, S. W., & Carman, G. P. (2004). Design of a piezoelectric-hydraulic pump with active valves. *Journal of Intelligent Material Systems and Structures*, 15(2), 107-115. <https://doi.org/10.1177/1045389X04039730>
- Li, H., Liu, J., Li, K., & Liu, Y. (2019). Piezoelectric micro-jet devices: A review. *Sensors and Actuators A: Physical*, 297, 111552. <https://doi.org/10.1016/j.sna.2019.111552>
- Liu, C., Zhu, Y., & Wu, C. (2020). Optimization of a synthetic jet based piezoelectric air pump and its application in electronic cooling. *Microsystem Technologies*, 26, 1905-1914. <https://doi.org/10.1007/s00542-019-04743-2>
- Liu, G., Shen, C., Yang, Z., Cai, X., & Zhang, H. (2010). A disposable piezoelectric micropump with high performance for closed-loop insulin therapy system. *Sensors and Actuators A: Physical*, 163(1), 291-296. <https://doi.org/10.1016/j.sna.2010.06.030>
- Lu, S., Yu, M., Qian, C., Deng, F., Chen, S., Kan, J., & Zhang, Z. (2020). A quintuple-bimorph tenfold-chamber piezoelectric pump used in water-cooling system of electronic chip. *Ieee Access*, 8, 186691-186698. <https://doi.org/10.1109/ACCESS.2020.3030247>
- Mohith, S., Karanth, P. N., & Kulkarni, S. M. (2019). Recent trends in mechanical micropumps and their applications: A review. *Mechatronics*, 60, 34-55. <https://doi.org/10.1016/j.mechatronics.2019.04.009>
- Ni, J., Xuan, W., Li, Y., Chen, J., Li, W., Cao, Z., & Luo, J. (2023). Analytical and experimental study of a valveless piezoelectric micropump with high flowrate and pressure load. *Microsystems & Nanoengineering*, 9(1), 72. <https://doi.org/10.1038/s41378-023-00547-7>
- Sakuma, S., Kasai, Y., Hayakawa, T., & Arai, F. (2017). On-chip cell sorting by high-speed local-flow control using dual membrane pumps. *Lab on a Chip*, 17(16), 2760-2767. <https://doi.org/10.1039/C7LC00536A>
- Sayar, E., & Farouk, B. (2012). Multifield analysis of a piezoelectric valveless micropump: effects of actuation frequency and electric potential. *Smart Materials and Structures*, 21(7), 075002. <https://dx.doi.org/10.1088/0964-1726/21/7/075002>
- Senjanović, I., Vladimir, N., & Tomić, M. (2016). On new

- first-order shear deformation plate theories. *Mechanics Research Communications*, 73, 31-38.
<https://doi.org/10.1016/j.mechrescom.2016.02.005>
- Singh, S., Kumar, N., George, D., & Sen, A. K. (2015). Analytical modeling, simulations and experimental studies of a PZT actuated planar valveless PDMS micropump. *Sensors and Actuators A: Physical*, 225, 81-94. <https://doi.org/10.1016/j.sna.2015.02.012>
- Takaddus, A. T., & Chandy, A. J. (2018). A three-dimensional (3D) two-way coupled fluid-structure interaction (FSI) study of peristaltic flow in obstructed ureters. *International Journal for Numerical Methods in Biomedical Engineering*, 34(10), e3122. <https://doi.org/10.1002/cnm.3122>
- Vante, A. B., & Kanish, T. C. (2024). Fluid-structure interaction and experimental studies of passive check valve based piezoelectric micropump for biomedical applications. *Advances in Materials and Processing Technologies*, 10(3), 2095-2121. <https://doi.org/10.1080/2374068X.2023.2206176>
- Wang, B., Chu, X., Li, E., & Li, L. (2006). Simulations and analysis of a piezoelectric micropump. *Ultrasonics*, 44, e643-e646. <https://doi.org/10.1016/j.ultras.2006.05.018>
- Wang, L., Chen, W., Liu, J., Deng, J., & Liu, Y. (2019). A review of recent studies on non-resonant piezoelectric actuators. *Mechanical Systems and Signal Processing*, 133, 106254. <https://doi.org/10.1016/j.ymsp.2019.106254>
- Wang, Y. N., & Fu, L. M. (2018). Micropumps and biomedical applications—A review. *Microelectronic Engineering*, 195, 121-138. <https://doi.org/10.1016/j.mee.2018.04.008>
- Yang, X., Zhou, Z., Cho, H., & Luo, X. (2006). Study on a PZT-actuated diaphragm pump for air supply for micro fuel cells. *Sensors and Actuators A: Physical*, 130, 531-536. <https://doi.org/10.1016/j.sna.2005.12.021>
- Yeming, S., & Junyao, W. (2019). Digitally-controlled driving power supply for dual-active-valve piezoelectric pump. *Microsystem Technologies*, 25(4), 1257-1265. <https://doi.org/10.1007/s00542-018-4101-1>
- Zeng, P., Li, L. A., Dong, J., Cheng, G., Kan, J., & Xu, F. (2016). Structure design and experimental study on single-bimorph double-acting check-valve piezoelectric pump. *Proceedings of the Institution of Mechanical Engineers, Part C: Journal of Mechanical Engineering Science*, 230(14), 2339-2344. <https://doi.org/10.1177/0954406215596357>
- Zhang, W., & Eitel, R. E. (2013). An integrated multilayer ceramic piezoelectric micropump for microfluidic systems. *Journal of Intelligent Material Systems and Structures*, 24(13), 1637-1646. <https://doi.org/10.1177/1045389X13483023>
- Zhao, D., He, L. P., Li, W., Huang, Y., & Cheng, G. M. (2019). Experimental analysis of a valve-less piezoelectric micropump with crescent-shaped structure. *Journal of Micromechanics and Microengineering*, 29(10), 105004. <https://doi.org/10.1088/1361-6439/ab3278>